

Effect of operating temperature on reverse solute flux in forward osmosis by incorporating the surface charge density

Luopeng Yang*, Dianchen Gai, Yongsheng Tian

School of Thermal Engineering, Shandong Jianzhu University, Jinan 250101, China, emails: yangluopeng19@sdjzu.edu.cn (L. Yang), gdc2022@163.com (D. Gai), tianyongsheng18@sdjzu.edu.cn (Y. Tian)

Received 4 December 2022; Accepted 23 March 2023

ABSTRACT

In order to investigate the effect of operating temperature on the reverse solute diffusion, the forward osmosis-only model incorporating the surface charge on solute partitioning is developed to obtain the reverse solute flux as a function of operating temperature and draw solution concentration using MATLAB. By comparing the calculated reverse solute flux for bulk draw solution concentrations at different operating temperatures, the range of the draw solution concentration at the support layer-active layer interface applicable to the constant surface charge density is found. The concentration beyond which the surface charge density is not constant, which is caused by the variety of the Debye length with the draw solution concentration, decreases with increasing operating temperature. The dilutive internal concentration polarization at 45°C is greater than that at 25°C due to the greater structural parameter and ratio of the structural parameter to diffusion coefficient at 45°C. The lower reverse solute flux at 45°C than that at 25°C is due to the fact that the ratio of the effective concentration between 25°C and 45°C outweighs that of the effective solute permeability coefficient.

Keywords: Operating temperature; Reverse solute flux; Surface charge density; Concentration polarization

1. Introduction

Forward osmosis (FO) is a kind of membrane separation technology that utilizes natural osmotic pressure as a driving force to make water pass through the membrane [1–3]. Compared with large-scale commercialized membrane technologies of reverse osmosis (RO) [4], nanofiltration [5], membrane distillation [6] and electrodialysis [7], FO is favored by the advantages of free of hydraulic pressure and ease of membrane cleaning [8]. FO has gained great attention in the industries of seawater desalination [9], wastewater recovery [10], osmotic membrane bioreactor [11], liquid food processing [12], etc. The complex reverse solute diffusion transport phenomenon, which is inherently linked with the water flux (J_w) and membrane fouling, has received

growing attention to obtain insight into developing an efficient forward osmosis membrane [13–16].

Extensive research has been conducted on the concentration polarization and membrane characteristic parameters of FO membrane. The membrane characteristic parameters of the pure water permeability coefficient (A), solute permeability coefficient (B) and structural parameter (S) [17,18], were mostly obtained by the RO-FO based test [19–22]. S was gained based on the measured A and B in the RO experiment [23]. Dilutive internal concentration polarization (ICP) and external concentration polarization (ECP) were calculated in term of the experimental membrane characteristic parameters together with the physical properties and flow conditions of the solution [24,25]. The mechanical damage on the thin FO membrane, which is caused by the imposed high pressure in the RO experiment, resulted in underestimating

* Corresponding author.

B and S [26,27]. The underestimation of B leads to underestimating the reverse solute flux (J_s) while the underestimation of S corresponds to underestimating ICP, leads to overrating J_s . For low concentrations of the draw solution, the opposite effects of underestimating B and S on J_s were counteracted. An increasing dilutive ICP and an unvarying B with an increasing concentration of the draw solution contribute to overrating J_s .

A FO-only model was proposed to improve the accuracy of membrane characteristic parameters in the RO-FO based test [26,28–30]. Therein, J_w and J_s for different draw solution concentrations in the FO experiment were nonlinearly fitted by the least-square method to obtain the membrane characteristic parameters. As the mere effect of the operation temperature (t) on membrane characteristic parameters were considered in the FO-only model, the ratio of B to A (B/A), which determines the ratio of J_s to J_w (J_s/J_w), is constant at constant t . The FO-only model restricts to the constant condition where the coefficient of variation (CV) of the experimental J_s/J_w is less than 10% [26]. The calculated J_s was 20% lower than the experimental at 25°C for the non-constant condition where the CV of the experimental J_s/J_w is greater than 10% [31]. As the CV of J_s/J_w decreases with increasing t [32], the FO-only model may be applicable at t below 25°C.

Directing at the above-mentioned non-constant condition, the electrostatic interactions between the membrane surface charge and draw solution solute were introduced to improve the accuracy of the calculated J in the FO-only model [31]. But the poorly calculated J_s with its determination coefficient of 79% occurs for a large zeta potential on the membrane surface. The surface charge on the solute partitioning was further introduced to the FO-only model [33]. It was proved that the variation of the solute partitioning in the active layer with the draw solution concentration was the key reason for the non-constant condition. Since the Poisson–Boltzmann equation, which calculates the surface charge density in term of the zeta potential, restricts to low concentrations of the draw solution at the support layer-active layer interface ($C_{d,m}$) [34,35], the high $C_{d,m}$ in the FO membrane exceeds the applicable range of the Poisson–Boltzmann equation. Coday et al. [36] found that the decrease in the zeta potential stabilizes till the Debye length, which decreases with an increase in the draw solution concentration, approaches the hydration radius of ions. The decreasing zeta potential with an increasing $C_{d,m}$ results in the constant surface charge density [31]. Therefore, there exists a critical draw solution concentration beyond which the surface charge density is not constant. As the assumed constant surface charge density in the FO-only model [33] was inapplicable to the $C_{d,m}$ beyond the critical one, the effect of the surface charge density on J_w and J_s was attributed to the membrane characteristic parameters. The inappropriate membrane characteristic parameters further affect the dilutive ICP which is the dominating concentration polarization [24]. Thus it is important to determine the critical draw solution concentration for accurately predicting the membrane characteristic parameters and concentration polarizations.

Little attention was paid to the effect of t on J_s regarding the FO-only model with the surface charge on solute partitioning. Compared with B [28–30], effective solute permeability coefficient (B^*), which is a function of B , average

partition coefficient ($P_{m,eff}/P_{f,m}$) and correction factor of diffusion coefficient, contributes to reliably predicting J_s as the electrostatic interactions of surface charges were taken into account [33]. The concentration polarization inherently relates to S , diffusion coefficient and solution properties [24,25]. The effect of t on these factors, which influence B^* and concentration polarization, act on J_s . Although J_s is small, the effect of t on J_s plays an important role in the membrane scaling and J_w [13]. B^* increases with an increase in t while S , which differs in the hydration radius of the draw solute [31], might increase rather than decreasing due to the different changing rates regarding the tortuosity and porosity of the support layer with an increasing t . Therefore, the recognized fact that J_s increases with increasing t depends on the draw solute.

The FO-only model, which incorporates the surface charge on the solute partitioning, is developed to predict J_s using MATLAB. By comparing the calculated J_s at different t and bulk draw solution concentrations, the range of $C_{d,m}$ applicable to the constant surface charge density is determined and analyzed. Thus, the application range of the FO-only model with the surface charge on solute partitioning, which has not been taken into account, is define. The effect of t on J_s is obtained by analyzing B^* and concentration polarizations.

2. Model

Fig. 1 shows the mass transfer process through the FO membrane layer. The membrane transport layer constitutes the draw boundary layer, support layer, active layer and feed boundary layer. A one-dimensional steady-state mass transfer process through the FO membrane layer is modeled with the following assumptions:

- The solute transport across the membrane is normal to the area of the active layer.
- There are continuous chemical potentials in the solution and membrane due to the chemical equilibrium at the interface of the solution and membrane [37].
- The surface charge density is constant [31,33].
- The effect of t on the surface charge density is negligible [38].

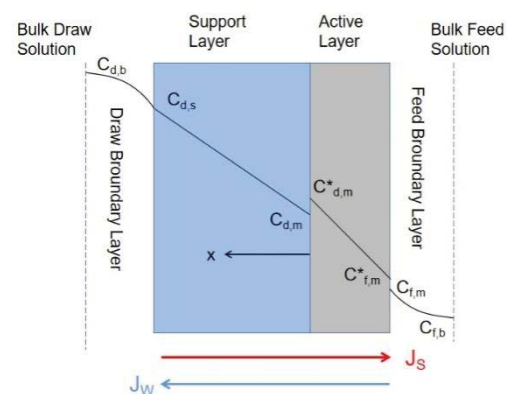


Fig. 1. Mass transfer through the forward osmosis membrane layer [30].

Fitted empirical polynomial equations of the diffusion coefficient (D) and osmotic pressure (π) are given by [32,39]:

$$D = a_0 + a_1C^{0.5} + a_2C + a_3C^{1.5} + a_4C^2 \quad (1)$$

$$\pi = a_{1,\pi}C + a_{2,\pi} \quad (2)$$

J_s within the draw boundary layer, support layer and feed boundary layer is expressed by:

$$J_s = D \frac{dC}{dx} - J_w C \quad (3)$$

The density and viscosity of the solution and diffusion coefficient of the solute in the boundary layer model are assumed to be constant and be equal to those of the bulk solution as the concentration differences within the thin boundary layer are small.

The feed solution concentration at the active layer-feed interface ($C_{f,m}$) and the draw solution concentration at the support layer-draw interface ($C_{d,s}$), which is obtained by integrating Eq. (3), is given by [25]:

$$C_{f,m} = C_{f,b} \exp\left(\frac{J_w}{k_f}\right) + \frac{J_s}{J_w} \left(\exp\left(\frac{J_w}{k_f}\right) - 1 \right) \quad (4)$$

$$C_{d,s} = C_{d,b} \exp\left(-\frac{J_w}{k_d}\right) + \frac{J_s}{J_w} \left(\exp\left(-\frac{J_w}{k_d}\right) - 1 \right) \quad (5)$$

where k_f and k_d are the mass transfer coefficient of the feed and the draw, respectively. The expression equation of k [25] is:

$$k = \frac{ShD}{d_h} \quad (6)$$

The expression equation of hydraulic diameter (d_h) is:

$$d_h = \frac{2WH}{W + H} \quad (7)$$

The Sherwood number (Sh) for the laminar flow can be calculated using:

$$Sh = 1.85 \left(ReSc \frac{d_h}{L} \right)^{0.33} \quad (8)$$

The Sherwood number (Sh) for the turbulent flow can be calculated using:

$$Sh = 0.04 Re^{0.75} Sc^{0.33} \quad (9)$$

The expression equation of Reynolds number (Re) is:

$$Re = \frac{\rho d_h v}{\mu} \quad (10)$$

The expression equation of Schmidt number (Sc) is:

$$Sc = \frac{\mu}{\rho D} \quad (11)$$

The diffusion coefficient in the support layer is not constant as the concentration difference within the thick support layer is large. Substituting D in Eq. (1) by Eq. (3), the expression is given by [31]:

$$\frac{dC}{dx} = \frac{J_s + J_w C(x)}{a_0 + a_1C^{0.5} + a_2C + a_3C^{1.5} + a_4C^2} \quad (12)$$

The boundary layer conditions of the support layer are:

$$\begin{aligned} C(x) &= C_{d,m}, x = 0 \\ C(x) &= C_{d,s}, x = S \end{aligned}$$

As it has been proven that the model with considering the surface charge has a higher accuracy of predicting J_s compared to the model without considering the surface charge [33], the following is the model with considering the surface charge.

J_s which is modified by the diffusion coefficient and potential in the active layer [33], is given by:

$$J_s = B^* (C_{d,m}^* - C_{f,m}^*) \quad (13)$$

The expression equation of B^* is:

$$B^* = B \frac{D_{eff}}{D_0} \frac{P_{m,eff}}{P_{f,m}} \quad (14)$$

The solute concentration in the active layer [33] is given by:

$$C_m^* = C_m \exp\left(-\frac{zF\phi_m^*}{RT}\right) \quad (15)$$

The relationship equation between the Donnan potential (ϕ_m^*) and surface charge density (σ_0) [40,41] is:

$$\phi_m^* = \frac{2RT}{zF} \operatorname{arcsinh} \left(\frac{\sigma_0}{\sqrt{8RT\epsilon_0\epsilon_r C_m}} \right) \quad (16)$$

The expression equation of $P_{m,eff}/P_{f,m}$ [33] is:

$$\frac{P_{m,eff}}{P_{f,m}} = \exp\left[-\frac{zF(\phi_m^{ave} - \phi_{f,m}^*)}{RT}\right] \quad (17)$$

The effective Donnan potential (φ_m^{ave}) in the active layer is expressed by:

$$\phi_m^{\text{ave}} = \frac{\int_{C_{f,m}}^{C_{d,m}} \phi_m^*}{C_{d,m} - C_{f,m}} \quad (18)$$

By inserting Eqs. (14)–(15) and (17) into Eq. (13), J_s is given as:

$$J_s = B \frac{D_{\text{eff}}}{D_0} \left(\exp \left(-\frac{zF(\phi_m^{\text{ave}} - \phi_{f,m}^*)}{RT} \right) \right) \left(C_{d,m} \exp \left(-\frac{zF\phi_{d,m}^*}{RT} \right) - C_{f,m} \exp \left(-\frac{zF\phi_{f,m}^*}{RT} \right) \right) \quad (19)$$

As $C_{d,m}$ is about 100 times of $C_{f,m}$, Eq. (20) can be simplified as:

$$J_s = B \frac{D_{\text{eff}}}{D_0} \left(C_{d,m} \exp \left(-\frac{zF(\phi_m^{\text{ave}} - \phi_{f,m}^* + \phi_{d,m}^*)}{RT} \right) \right) \quad (20)$$

J_w , which is modified by the water partition coefficient (P_w) [33], is given by:

$$J_w = AP_w (\pi_{d,m} - \pi_{f,m}) \quad (21)$$

The global error (E) is expressed by [26]:

$$E = \sum_i^n \left(\frac{J_{w,i}^{\text{exp}} - J_{w,i}^{\text{model}}}{J_w^{\text{exp},n}} \right)^2 + \sum_i^n \left(\frac{J_{s,i}^{\text{exp}} - J_{s,i}^{\text{model}}}{J_s^{\text{exp},n}} \right)^2 \quad (22)$$

The water flux determination coefficient (R_w^2) and solute flux determination coefficient (R_s^2) are given by [26]:

$$R_w^2 = 1 - \frac{\sum_i^n (J_{w,i}^{\text{exp}} - J_{w,i}^{\text{model}})^2}{\sum_i^n (J_{w,i}^{\text{exp}} - \overline{J_w^{\text{exp},n}})^2} \quad (23)$$

$$R_s^2 = 1 - \frac{\sum_i^n (J_{s,i}^{\text{exp}} - J_{s,i}^{\text{model}})^2}{\sum_i^n (J_{s,i}^{\text{exp}} - \overline{J_s^{\text{exp},n}})^2} \quad (24)$$

A simplified flowchart of the computation program is shown in Fig. 2. Based on input data and initial guesses of A , B and S , the program calculates the model fluxes of $J_{w,i}^{\text{model}}$ and $J_{s,i}^{\text{model}}$ by Eqs. (4) and (5), (12), (15), (20) and (21). The membrane characteristic parameters of A , B and S are optimized by the minimization of E in Eq. (22). R_w^2 and R_s^2 are calculated by Eqs. (23) and (24).

3. Results and discussion

3.1. Model verification

The commercial CTA membrane using KCl as the draw solution and deionized water as the feed solution is calculated based on the experimental conditions in Table 1 [31,32]. The empirical coefficients for D [39] and π [32] of KCl at different t are detailed below in Tables 2 and 3, respectively. The density and dynamic viscosity of KCl solution at different operating temperatures and concentrations are shown in Table 4 [32]. The calculated membrane characteristic parameters as well as R_w^2 and R_s^2 , which are based on the experimental data of J_w and J_s for the bulk draw solution concentrations of 0.5, 1, 1.5 and 2, are shown in Tables 5 and 6, respectively. A comparison of FO experimental and calculated results is shown in Table 7.

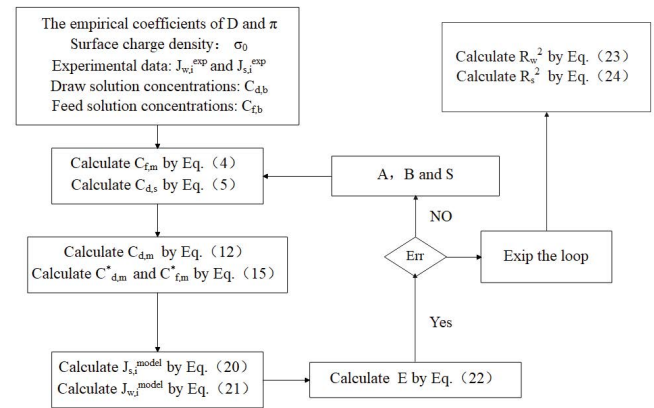


Fig. 2. Flowchart of the computation program.

Table 1
Experimental conditions [31,32]

Experimental condition	Description	Unit	Value
L	Channel length	m	0.077
W	Channel width	m	0.026
H	Channel depth	m	0.003
v	Cross-flow	m/s	0.085
h	Run time	h	6
t	Operating temperature	°C	25°C, 35°C, 45°C
σ_0	Surface charge density	C/m ²	-9.8×10^{-4}

Table 2
Empirical coefficients for diffusion coefficient of KCl at different operating temperatures [39]

t (°C)	$a_0 \times 10^{-9}$	$a_1 \times 10^{-9}$	$a_2 \times 10^{-9}$	$a_3 \times 10^{-9}$	$a_4 \times 10^{-9}$	R^2
25	1.99	-0.74	1.16	-0.65	0.15	0.99
35	2.45	-0.84	1.28	-0.71	0.15	0.99
45	2.96	-1.14	1.77	-0.88	0.14	0.99

Table 3
Empirical coefficients for osmotic pressure of KCl at different operating temperatures [32]

t (°C)	$a_{1,\pi}$	$a_{2,\pi}$	R^2
25	46.86	-0.81	0.99
35	48.66	-1.64	0.99
45	49.96	-1.91	0.99

Table 4
Density and viscosity of KCl solution at different operating temperatures and concentrations

t (°C)	C_{fb} (M)	$\rho \times 10^3$ (kg/m ³)	$\mu \times 10^{-3}$ (kg/(m·s))
25	0.0	0.998	0.892
	0.5	1.021	0.891
	1.0	1.042	0.887
	1.5	1.064	0.892
	2.0	1.086	0.895
	3.0	1.129	0.912
35	0.0	0.995	0.723
	0.5	1.017	0.726
	1.0	1.039	0.733
	1.5	1.060	0.740
	2.0	1.082	0.748
	3.0	1.125	0.768
45	0.0	0.991	0.597
	0.5	1.013	0.604
	1.0	1.035	0.614
	1.5	1.056	0.624
	2.0	1.077	0.635
	3.0	1.120	0.657

Table 5
Calculated membrane characteristic parameters at different operating temperatures

t (°C)	A (L/m ² ·h·bar)	B (L/m ² ·h)	S (μm)
25	0.26	0.32	90.0
35	0.33	0.24	209.3
45	0.44	0.41	247.1

It could be seen in Table 5 that S at 35°C and 45°C is 2.32 and 2.74 times of that at 25°C, respectively while A and B at 35°C and 45°C were less than 1.70 times of those at 25°C. The parameters of A and B regarding the active layer directly affect J_w and J_s . The influence factor on J_w and J_s in the support layer is the ratio of S to D (S/D). A , B and S , which are obtained simultaneously in the computation program, exert equal weights on J_w and J_s . The variation of S with an increasing t is greater than that of A and B as D increases with the increasing t .

R_w^2 and R_s^2 at 25°C, 35°C and 45°C in Table 6 are up to 96% except R_s^2 at 45°C. A comparison of the calculated J_s with the experimental one at different t is presented in

Table 6
Determination coefficients at different operating temperatures

t (°C)	R_w^2 (%)	R_s^2 (%)
25	97.8	96.0
35	99.8	97.7
45	99.2	86.9

Table 7
Comparison of forward osmosis experimental and calculated results

t (°C)	C_{fb} (M)	J_w^{exp} (L/m ² ·h)	J_w^{model} (L/m ² ·h)	J_s^{exp} (mmol/m ² ·h)	J_s^{model} (mmol/m ² ·h)
25	0.5	5.98	5.32	97.2	94.7
	1.0	9.86	9.16	162.0	184.1
	1.5	12.12	12.33	248.4	262.8
	2.0	15.16	15.08	363.6	333.9
	3.0	19.23	19.75	471.6	460.4
	0.5	6.41	6.51	56.3	56.9
35	1.0	10.76	10.70	109.6	108.7
	1.5	14.22	13.96	167.4	151.7
	2.0	16.90	16.68	190.3	189.0
	3.0	21.27	21.14	274.0	252.6
	0.5	8.32	8.35	126.0	103.2
	1.0	13.53	13.46	207.0	186.3
45	1.5	17.24	17.35	216.0	253.3
	2.0	21.41	20.53	308.9	310.2
	3.0	27.18	25.56	443.1	403.3

Fig. 3. The comparison in Fig. 3 indicates a good agreement between the predictions and experimental data. The deviation occurs for a bulk draw solution concentration of 1.5 M at 45°C shown in Fig. 3c. It could be seen that the measured J_s for 1.5 M approximately equals to that for 1 M. As J_s increases with an increase in the bulk draw solution concentration, the underestimated J_s for 1.5 M accounts for the deviation. R_s^2 at 45°C increases from 86.9% to 95% if the underestimated J_s for 1.5 M is not taken into account, and the recalculated R_s^2 is within the acceptable range. The good agreement demonstrates that the experimental membrane characteristic parameters in Table 5 can accurately describe the inherent properties of the FO membrane.

In order to determine the $C_{d,m}$ range applicable to the constant surface charge density, J_w and J_s for the bulk draw solution concentration of 3 M are obtained by extrapolating from the experimental membrane characteristic parameters in Table 5. The relative deviations of J_w and J_s between the experimental data and predictions are shown in Table 8. It can be found that the relative deviation of J_s at 35°C and 45°C is obviously greater than that at 25°C. This implies that $C_{d,m}$ for the bulk draw solution concentration of 3 M at 35°C and 45°C is beyond its range applicable to the constant surface charge density.

The reason for the critical draw solution concentration, beyond which the constant surface charge density is

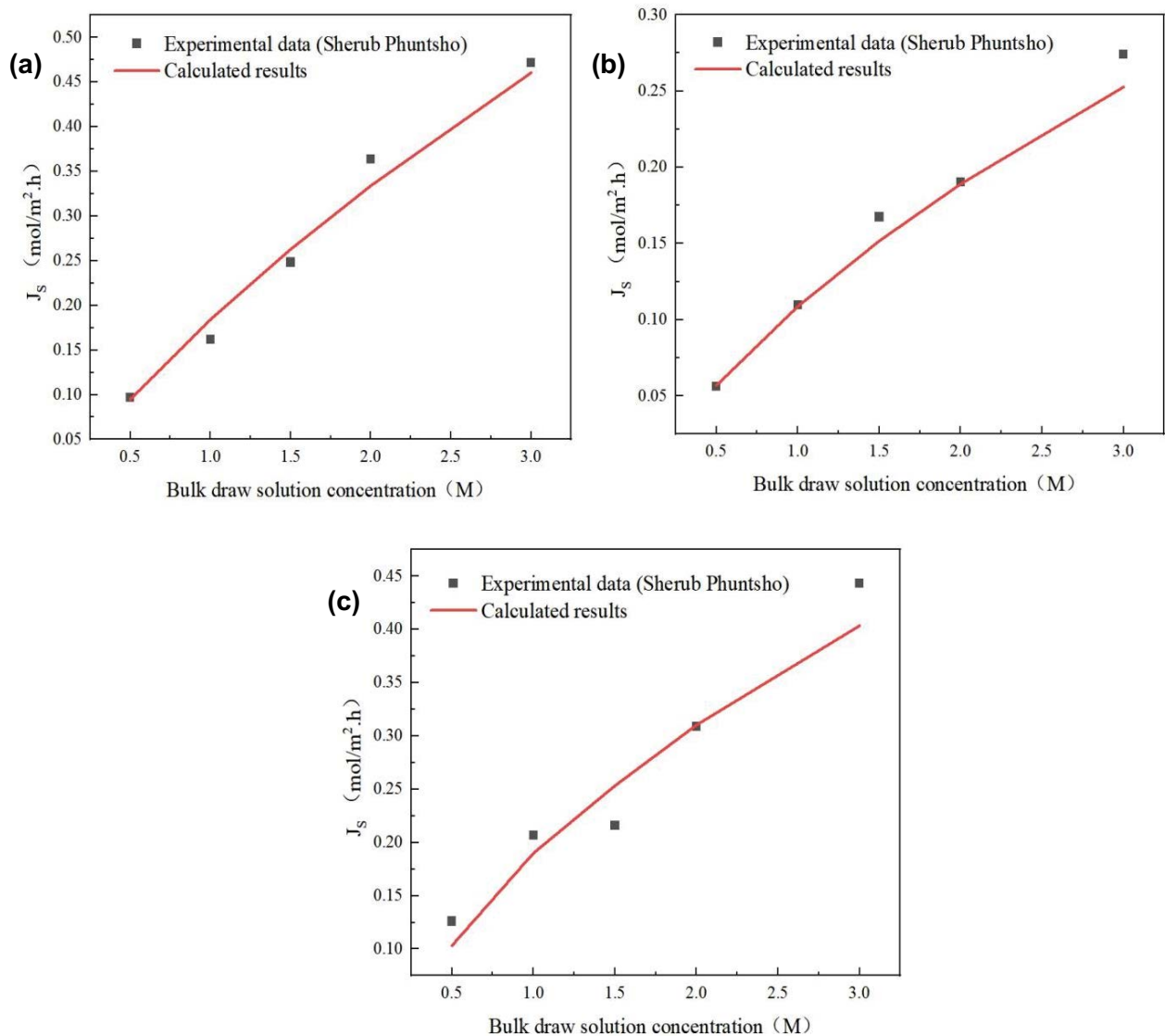


Fig. 3. Comparison of the experimental and calculated J_s at different t (a) 25°C, (b) 35°C and (c) 45°C.

Table 8

Relative deviations of the J_w and J_s at different operating temperatures for 3 M

t (°C)	Relative deviation of J_w (%)	Relative deviation of J_s (%)
25	2.7	2.4
35	0.6	7.8
45	4.3	9.0

inapplicable, is the variety of the Debye length with $C_{d,m}$. As the CTA membrane surface is mainly composed of non-ionogenic hydroxyl and acetoxy functional groups, accumulating anions on the membrane surface leads to a negative zeta potential [42]. $C_{d,m}$ applicable to the Poisson–Boltzmann equation is restricted to a relatively narrow range [34,35]. The zeta potential stabilizes till the decreasing Debye length

approaches the hydration radius of the potassium ion with an increase in $C_{d,m}$ [36]. The constant zeta potential leads to a decreasing surface charge density with a further increase in $C_{d,m}$ [43]. The decreasing surface charge density results from the enhancing effects of binding potassium ions in the diffusion layer to the anions in the Stern layer [32,44,45]. Therefore, the critical draw solution concentration corresponds to the maximum $C_{d,m}$ for the constant surface charge density.

$\varphi_{f,m}^*$ is the dominating factor of J_s in Eq. (20) as $\varphi_{f,m}^*$ is much greater than $\varphi_{d,m}^*$ and φ_m^{ave} due to the fact that $C_{d,m}$ is two orders of magnitude larger than $C_{f,m}$, and that D_{eff}/D_0 hardly changes with the bulk draw solution concentration [33]. Thus, a decrease in the surface charge density results in an increase in J_s due to decreasing $\varphi_{f,m}^*$. The phenomenon that the decreasing surface charge density occurs for the bulk draw solution concentration of 3 M at 35°C and 45°C is proved in Fig. 3b and c by the fact that the calculated J_s

which is obtained by the constant surface charge density, is apparently less than the experimental one.

The calculated $C_{d,m}$ at different t for the bulk draw solution concentration of 2 M and 3 M is compared in Fig. 4. As it is proved in Fig. 3 that all of the calculated $C_{d,m}$ are less than their corresponding critical draw solution concentrations except the ones for 3M at 35°C and 45°C, it is inferred in Fig. 4 that the critical draw solution concentration at 25°C is greater than 1.69 M, and that the critical one is in the range of 1.04 to 1.33 M at 35°C and 0.94 to 1.18 M at 45°C, respectively. Compared with the constant surface charge density, the surface charge density for 3 M is extrapolated by the experimental J_s , decreases by 49% at 35°C and 79% at 45°C, respectively. Compared with at 35°C, the greater decreasing percentage of the surface charge density at 45°C, which is positively correlated with the difference between the critical draw solution concentration and $C_{d,m}$ [38], together with the lower $C_{d,m}$ results in the lower

critical draw solution concentration. This can be explained by the fact that a decrease in the Debye length with increasing t [36] contributes to decreasing the critical draw solution concentration at the condition of the close size between the Debye length and hydration radius of solute ion.

3.2. Effect of concentration polarization on J_s at different operating temperatures

An ideal forward osmosis process requires high water flux, low reverse solute flux and low fouling characteristics. A low J_s contributes to decreasing membrane fouling [46], thus enhancing J_w . A comparison of the calculated J_w and J_s at 25°C and 45°C is shown in Fig. 5. It can be seen that J_s at 45°C is lower than that at 25°C, and that the difference increases with increasing bulk draw solution concentration. This is contrary to the recognized fact that J_s increases with increasing t due to the combing effects of increasing solute permeability coefficient [24] and decreasing concentration polarization [32].

The concentration polarization, which tends to reduce the effective osmotic pressure difference in FO process, includes the dilutive external concentration polarization (DECP) on draw side, dilutive ICP in the support layer, and concentrative external concentration polarization (CECP) on feed side shown in Fig. 1. Compared with the dilutive ICP and DECP, the CECP is negligible. The effective concentration of solute transport across the active layer of the membrane is the concentration difference within the active layer of the membrane due to the Donnan potential. The proportions of the DECP, dilutive ICP and effective concentration are quantified by Eqs. (25)–(27) [47]:

$$\text{DECP} = \frac{C_{d,b} - C_{d,s}}{C_{d,b} - C_{f,b}} \times 100 \quad (25)$$

$$\text{Dilutive ICP} = \frac{C_{d,s} - C_{d,m}}{C_{d,b} - C_{f,b}} \times 100 \quad (26)$$

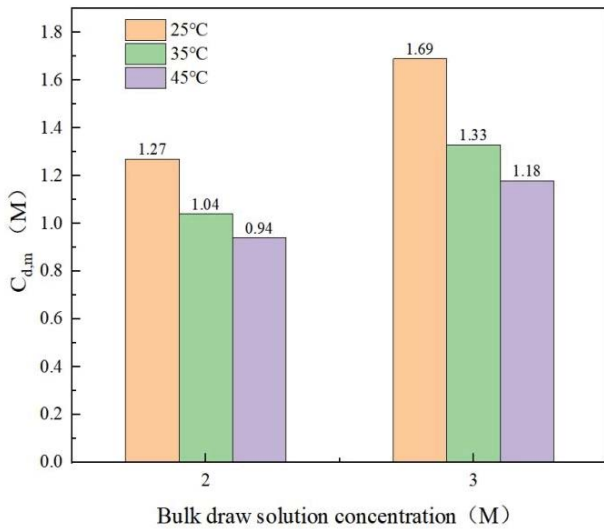


Fig. 4. Profiles of $C_{d,m}$ at different t for 2 M and 3 M.

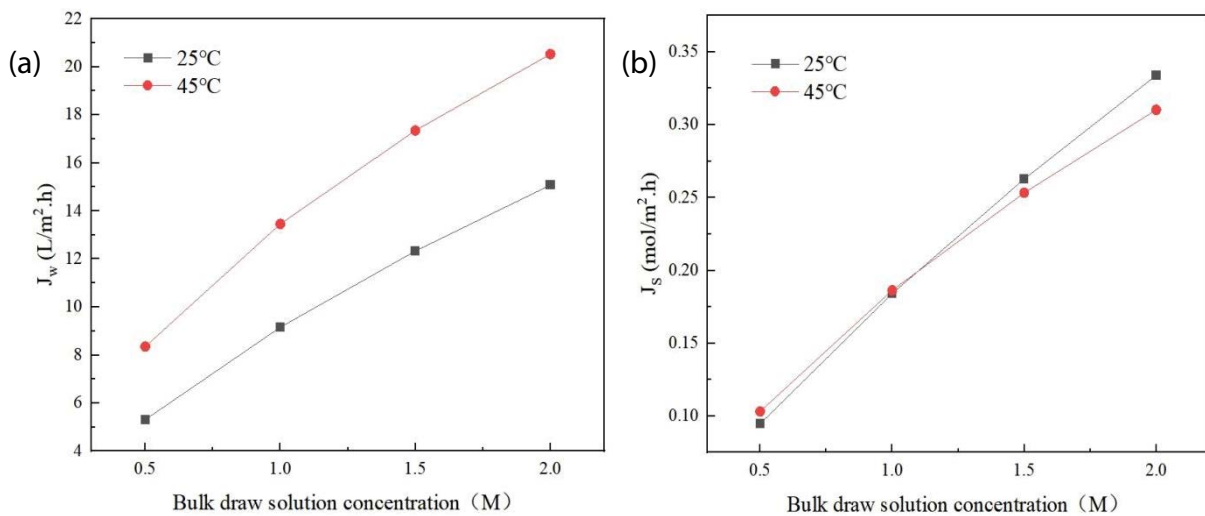


Fig. 5. Profiles of calculated (a) J_w and (b) J_s at 25°C and 45°C.

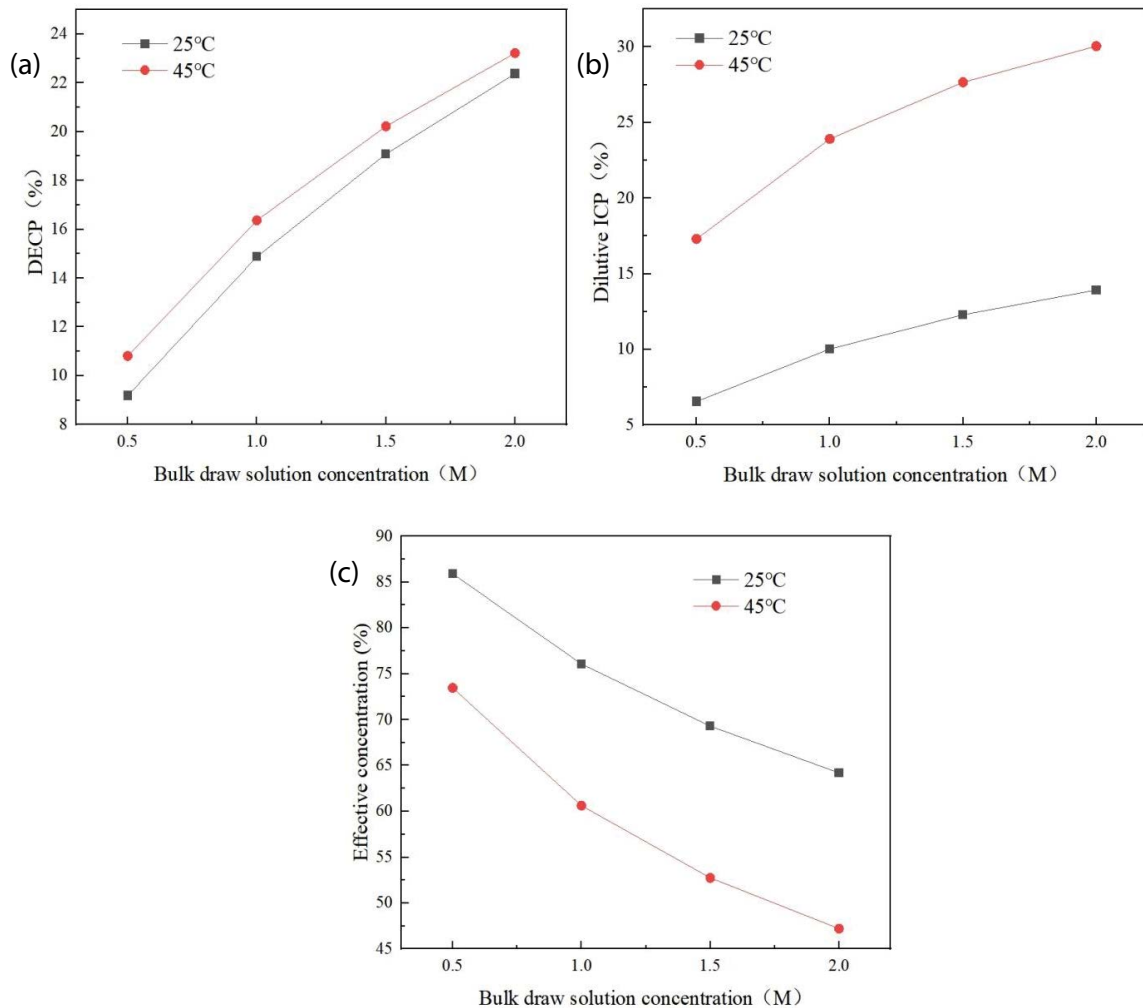


Fig. 6. Profiles of concentration polarizations and effective concentration at 25°C and 45°C (a) dilutive external concentration polarization, (b) dilutive internal concentration polarization and (c) effective concentration.

$$\text{Effective concentration} = \frac{C_{d,m}^* - C_{f,m}^*}{C_{d,b} - C_{f,b}} \times 100 \quad (27)$$

The proportion profiles with respect to the bulk draw solute concentration at 25°C and 45°C are presented in Fig. 6. It is shown in Fig. 6a that DECP at 45°C is greater than that at 25°C. The variation of DECP with t is consistent with the prior experimental results of Bui et al. [24]. With an increase in t , a notable increase in J_w causes by the increasing diffusion coefficient of water molecules, results in obviously increasing DECP while a slight increase in J_s due to a decreasing mass transfer resistance of the draw solute in the draw boundary layer causes a marginally decreasing DECP [48]. The outweighing effect of J_w on DECP accounts for the increasing DECP.

It is found in Fig. 6b that the dilutive ICP at 25°C is less than that at 45°C, which is inconsistent with the experimental result [20,24]. It is due the fact that the calculated S , which represents the mass transfer resistance in the support layer, based on the calculated data in Table 5 increases

with increasing t . The fact is proved by the Xie's et al. FO experimental results [49]. An increase in the porosity (ϵ) with the increasing t [50] contributes to accelerate the solute diffusion through the support layer. An increase in the tortuosity (τ) due to the thermal expansion effect results in increasing solute transport length. According to the correlation of τ and ϵ [28], the enhancing rate of τ outweighs that of ϵ , which accounts for the increasing S . The ratio of S to D (S/D), which is the determining factor of the dilutive ICP [24], at 45°C is found to be 1.84 times of that at 25°C based on the calculated S in Table 5 and calculated diffusion coefficients [39]. Thus, the dilutive ICP at 45°C is strengthened.

It can be seen in Fig. 6c that the effective concentration at 25°C is greater than that at 45°C, and that the ratio of the effective concentration between the 25°C and 45°C increases from 1.17 for 0.5 M to 1.36 for 2 M. This phenomenon is contrary to the previous results that the total concentration polarization decreases with increasing t [17,21]. The increasing ratio is due to fact that the great J_w at 45°C results in the high increasing gradients of dilutive ICP and DECP compared with at 25°C. According to the B^* in Fig. 7, the

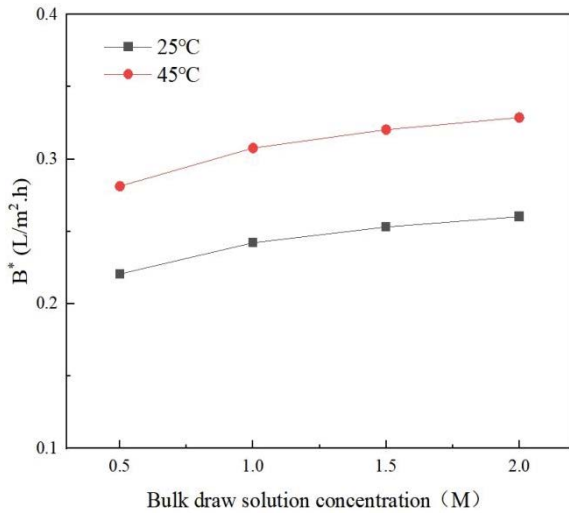


Fig. 7. Profiles of B^* with respect to bulk draw solution concentration at 25°C and 45°C.

calculated ratio of B^* between 25°C and 45°C almost keeps to be 1.27 for different bulk draw solution concentrations. It accounts for the low J_s at 45°C that the ratio of the effective concentration outweighs that of B^* .

4. Conclusions

The FO-only model incorporating the surface charge on solute partitioning is developed to obtain the reverse draw solute flux as a function of operation temperature and bulk draw solution concentration. The accuracy of the mathematical model is proved by the good agreement between the calculated results and experimental data.

By comparing the calculated reverse solute flux at different operation temperatures and bulk draw solution concentrations, the range of the draw solution concentration at the support layer-active layer interface applicable to the constant surface charge density is found. The critical draw solution concentration, which is caused by the variety of the Debye length with the draw solution concentration at the support layer-active layer interface, decreases with increasing operating temperature.

The dilutive external concentration polarization at 45°C is greater than that at 25°C due to the outweighing effect of water flux against the slight effect of reverse solute flux. The dilutive internal concentration polarization at 45°C is greater than that at 25°C due to the greater structural parameter and ratio of structural parameter and diffusion coefficient at 45°C. The lower reverse solute flux at 45°C than that at 25°C is due to the fact that the ratio of the effective concentration between 25°C and 45°C outweighs that of the effective solute permeability coefficient.

Acknowledgements

This work was supported by the National Naturally Science Foundation of China (No. 51976022) and the Research Leader's Studio Project of Universities and Institutes in Jinan. The authors wish to thank all who assisted in conducting this work.

Declarations

Conflict of interest: The authors emphasize that there are no conflicts of interest about the publication of this article.

Symbols

A	— Pure water permeability coefficient, L/m ² ·h·bar
B	— Solute permeability coefficient, L/m ² ·h
B^*	— Effective solute permeability coefficient, L/m ² ·h
C	— Solution concentration, M (mol/L)
$C_{d,b}$	— Bulk draw solution concentration, M (mol/L)
$C_{d,s}$	— Draw solution concentration at the support layer-draw interface, M (mol/L)
$C_{d,m}$	— Draw solution concentration at the support layer-active layer interface, M (mol/L)
$C_{f,m}$	— Feed solution concentration at the active layer-feed interface, M (mol/L)
$C_{f,b}$	— Feed solution concentration in the bulk solution, M (mol/L)
C_m	— Concentration near the surface of active layer, M (mol/L)
C_m^*	— Solute concentration inside active layer, M (mol/L)
$C_{d,m}^*$	— Solute concentration at inside of active layer-draw interface, M (mol/L)
$C_{f,m}^*$	— Solute concentration at inside of active layer-feed interface, M (mol/L)
d_h	— Hydraulic diameter, m
D	— Diffusion coefficient of the draw solution, m ² /s
D^{eff}	— Effective diffusion coefficient, m ² /s
D_0	— Reference diffusion coefficient, m ² /s
E	— Global minimum error
J_w	— Water flux, L/m ² ·h
J_w^{exp}	— Experimental value of water flux, L/m ² ·h
$\overline{J_w^{\text{exp},n}}$	— Mean experimental water flux, L/m ² ·h
J_w^{model}	— Prediction value of water flux, L/m ² ·h
J_s	— Reverse draw solute flux, mol/m ² ·h
$J_{s,i}^{\text{exp}}$	— Experimental value of reverse solute flux, mol/m ² ·h
$\overline{J_s^{\text{exp},n}}$	— Mean experimental reverse solute flux experimental, mol/m ² ·h
$J_{s,i}^{\text{model}}$	— Prediction value of reverse solute flux, mol/m ² ·h
k	— Mass transfer coefficient, m/s
k_d	— Mass transfer coefficient of the draw, m/s
k_f	— Mass transfer coefficient of the feed, m/s
n	— Number of forward osmosis experiments
P_w	— Partition coefficient of water
$P_{m,\text{eff}}/P_{f,m}$	— Average partition coefficient
R	— Ideal gas constant (=8.314), J/mol·K
Re	— Reynolds number
R_w^2	— Determination coefficient of water flux
R_s^2	— Determination coefficient of reverse solute flux
S	— Structural parameter, μm
Sc	— Schmidt number
Sh	— Sherwood number
T	— Absolute temperature, K
t	— Operation temperature, °C

Greek

α_i	— Empirical coefficient of diffusion coefficient
$\alpha_{i,\pi}$	— Empirical coefficient of osmotic pressure
δ_a	— Thickness of the active layer, μm
ε	— Porosity of the support layer
ε_0	— Vacuum permittivity
ε_r	— Relative permittivity
μ	— Viscosity, $\text{kg}/(\text{m}\cdot\text{s})$
π	— Osmotic pressure, bar
ρ	— Density, kg/m^3
σ_0	— Surface charge density, C/m^2
τ	— Tortuosity of the support layer
τ	— Viscosity, $\text{mPa}\cdot\text{s}$
φ_m^*	— Donnan potential, mV
$\varphi_{f,m}^*$	— Donnan potential at inside of active layer-feed interface, mV
$\varphi_{d,m}^*$	— Donnan potential at inside of active layer-draw interface, mV
φ_m^{ave}	— Effective Donnan potential, mV

References

- [1] I. Chaoui, I. Ndiaye, S. Abderafi, S. Vaudreuil, T. Bounahmidi, Evaluation of FO membranes performance using a modelling approach, *Desal. Water Treat.*, 223 (2021) 71–98.
- [2] M. Damirchi, I. Koyuncu, Nutrient recovery from concentrated municipal wastewater by forward osmosis membrane and MgCl_2 based draw solution, *Desal. Water Treat.*, 211 (2021) 448–455.
- [3] M.H. Salih, A.F. Al-Alawy, A novel forward osmosis for treatment of high-salinity East Baghdad oilfield produced water as a part of a zero liquid discharge system, *Desal. Water Treat.*, 248 (2022) 18–27.
- [4] A. Pervov, T. Shirkova, V. Frenkel, New technology to treat leachate by low pressure reverse osmosis, *Desal. Water Treat.*, 259 (2022) 338–346.
- [5] S. Belhamidi, S. El-Ghazel, M. Taky, A. Elmidaoui, Nitrate removal of groundwater by reverse osmosis, nanofiltration and electrodialysis: performances and cost comparison, *Desal. Water Treat.*, 262 (2022) 230–243.
- [6] W. Alam, M. Asif, M. Suleman, Techno-economic evaluation of multi-stage vacuum membrane distillation (MSVMD), *Desal. Water Treat.*, 230 (2021) 64–79.
- [7] B.M.B. Ensano, Y. Ahn, Reverse electrodialysis for perchlorate abatement in salt water, *Desal. Water Treat.*, 230 (2021) 129–135.
- [8] W.A. Suwaileh, D.J. Johnson, S. Sarp, N. Hilal, Advances in forward osmosis membranes: altering the sub-layer structure via recent fabrication and chemical modification approaches, *Desalination*, 436 (2018) 176–201.
- [9] W.L. Song, S.Y. Liu, M. Xie, P. Zhao, X.H. Wang, FO process for simultaneous wastewater pre-concentration and seawater concentrate disposal: impacts of seawater concentrate on membrane fouling in long-term operation, *Desalination*, 544 (2022) 116143, doi: 10.1016/j.desal.2022.116143.
- [10] J.E. Kim, S. Phuntsho, S.M. Ali, J.Y. Choi, H.K. Shon, Forward osmosis membrane modular configurations for osmotic dilution of seawater by forward osmosis and reverse osmosis hybrid system, *Water Res.*, 128 (2018) 183–192.
- [11] M.C. Yao, L. Duan, Y.H. Song, S.W. Hermanowicz, Degradation mechanism of Ibuprofen via a forward osmosis membrane bioreactor, *Bioresour. Technol.*, 321 (2021) 124448, doi: 10.1016/j.biortech.2020.124448.
- [12] Z.H. Li, S.J. Xiao, Q.M. Xiong, C.D. Wu, J. Huang, R.Q. Zhou, Y. Jin, Assessment of highly concentrated pear juice production through single-run forward osmosis using sodium lactate as the draw solute, *J. Food Eng.*, 333 (2022) 111122, doi: 10.1016/j.jfoodeng.2022.111122.
- [13] N. Akther, A. Sodiq, A. Giwa, S. Daer, H.A. Arafat, S.W. Hasan, Recent advancements in forward osmosis desalination: a review, *Chem. Eng. J.*, 281 (2015) 502–522.
- [14] Y.Y. Fang, L.X. Bian, X.L. Wang, Understanding membrane parameters of a forward osmosis membrane based on nonequilibrium thermodynamics, *J. Membr. Sci.*, 437 (2013) 72–81.
- [15] G.L. Qiu, G.K.W. Wong, Y.P. Ting, Electrostatic interaction governed solute transport in forward osmosis, *Water Res.*, 173 (2020) 115590, doi: 10.1016/j.watres.2020.115590.
- [16] W. Cheng, X.L. Lu, Y. Yang, J. Jiang, J. Ma, Influence of composition and concentration of saline water on cation exchange behavior in forward osmosis desalination, *Water Res.*, 137 (2018) 9–17.
- [17] S.J. You, X.H. Wang, M. Zhong, Y.J. Zhong, C. Yu, N.Q. Ren, Temperature as a factor affecting transmembrane water flux in forward osmosis: steady-state modeling and experimental validation, *Chem. Eng. J.*, 198–199 (2012) 52–60.
- [18] Y. Kim, S. Lee, H.K. Shon, S. Hong, Organic fouling mechanisms in forward osmosis membrane process under elevated feed and draw solution temperatures, *Desalination*, 355 (2015) 169–177.
- [19] Q. Wang, Z.Y. Zhou, J.Q. Li, Q.C. Tang, Y.X. Hu, Modeling and measurement of temperature and draw solution concentration induced water flux increment efficiencies in the forward osmosis membrane process, *Desalination*, 452 (2019) 75–86.
- [20] M.C.Y. Wong, K. Martinez, G.Z. Ramon, E.M.V. Hoek, Impacts of operating conditions and solution chemistry on osmotic membrane structure and performance, *Desalination*, 287 (2012) 340–349.
- [21] M. Shibuya, M. Yasukawa, T. Takahashi, T. Miyoshi, M. Higa, H. Matsuyama, Effect of operating conditions on osmotic-driven membrane performances of cellulose triacetate forward osmosis hollow fiber membrane, *Desalination*, 362 (2015) 34–42.
- [22] P. Zhao, B.Y. Gao, Q.Y. Yue, S.C. Liu, H.K. Shon, Effect of high salinity on the performance of forward osmosis: water flux, membrane scaling and removal efficiency, *Desalination*, 378 (2016) 67–73.
- [23] B. Kim, G. Gwak, S. Hong, Review on methodology for determining forward osmosis (FO) membrane characteristics: water permeability (A), solute permeability (B), and structural parameter (S), *Desalination*, 422 (2017) 5–16.
- [24] N.N. Bui, J.T. Arena, J.R. McCutcheon, Proper accounting of mass transfer resistances in forward osmosis: improving the accuracy of model predictions of structural parameter, *J. Membr. Sci.*, 492 (2015) 289–302.
- [25] C. Suh, S. Lee, Modeling reverse draw solute flux in forward osmosis with external concentration polarization in both sides of the draw and feed solution, *J. Membr. Sci.*, 427 (2013) 365–374.
- [26] A. Tiraferrri, N.Y. Yip, A.P. Straub, S.R.V. Castrillon, M. Elimelech, A method for the simultaneous determination of transport and structural parameters of forward osmosis membranes, *J. Membr. Sci.*, 444 (2013) 523–538.
- [27] J. Lee, J.Y. Choi, J.S. Choi, K.H. Chu, Y. Yoon, S. Kim, A statistics-based forward osmosis membrane characterization method without pressurized reverse osmosis experiment, *Desalination*, 403 (2017) 36–45.
- [28] M.R. Bilad, L. Qing, A.G. Fane, Non-linear least-square fitting method for characterization of forward osmosis membrane, *J. Water Process Eng.*, 25 (2018) 70–80.
- [29] J.T. Martin, G. Kolliopoulos, V.G. Papangelakis, An improved model for membrane characterization in forward osmosis, *J. Membr. Sci.*, 598 (2020) 117668, doi: 10.1016/j.memsci.2019.117668.
- [30] W.-J. Kim, D.R. Heldman, A mathematical estimation of the structural parameter for prediction of forward osmosis (FO) performance, *J. Water Process Eng.*, 39 (2020) 101719, doi: 10.1016/j.jwpe.2020.101719.
- [31] A.K.H. D'Haese, M.M. Mota, P. van der Meer, A.R.D. Verliefde, A refined draw solute flux model in forward osmosis: theoretical considerations and experimental validation, *J. Membr. Sci.*, 522 (2017) 316–331.

- [32] S. Phuntsho, S. Vigneswaran, J. Kandasamy, S. Hong, S. Lee, H.K. Shon, Influence of temperature and temperature difference in the performance of forward osmosis desalination process, *J. Membr. Sci.*, 415–416 (2012) 734–744.
- [33] R.S. Adha, T.-T. Nguyen, C. Lee, J. Jang, I.S. Kim, An improved perm-selectivity prediction of forward osmosis membrane by incorporating the effect of the surface charge on the solute partitioning, *J. Membr. Sci.*, 629 (2021) 119303, doi: 10.1016/j.memsci.2021.119303.
- [34] E.Y. Kim, S.C. Kim, Electrostatic interaction of charged surfaces with semipermeable membranes, *J. Korean Phys. Soc.*, 68 (2016) 658–667.
- [35] A. Martín-Molina, R. Hidalgo-Álvarez, M. Quesada-Pérez, Additional considerations about the role of ion size in charge reversal, *J. Phys.: Condens. Matter*, 21 (2009) 424105, doi: 10.1088/0953-8984/21/42/424105.
- [36] B.D. Coday, T. Luxbacher, A.E. Childress, N. Almaraz, P. Xu, T.Y. Cath, Indirect determination of zeta potential at high ionic strength: specific application to semipermeable polymeric membranes, *J. Membr. Sci.*, 478 (2015) 58–64.
- [37] Z.H. Foo, D. Rehman, O.Z. Coombs, A. Deshmukh, J.H. Lienhard V, Multicomponent Fickian solution-diffusion model for osmotic transport through membranes, *J. Membr. Sci.*, 640 (2021) 119819, doi: 10.1016/j.memsci.2021.119819.
- [38] A. Al-Amoudi, P. Williams, S. Mandale, R.W. Lovitt, Cleaning results of new and fouled nanofiltration membrane characterized by zeta potential and permeability, *Sep. Purif. Technol.*, 54 (2006) 234–240.
- [39] V.M.M. Lobo, Mutual diffusion coefficients in aqueous electrolyte solutions, *Pure Appl. Chem.*, 65 (1993) 2613–2640.
- [40] D.C. Grahame, The electrical double layer and the theory of electrocapillarity, *Chem. Rev.*, 41 (1947) 441–501.
- [41] H. Ohshima, *Biophysical Chemistry of Biointerfaces*, John Wiley & Sons, Japan, 2010.
- [42] S. Muthu, A. Childress, J. Brant, Propagation-of-uncertainty from contact angle and streaming potential measurements to XDLVO model assessments of membrane–colloid interactions, *J. Colloid Interface Sci.*, 428 (2014) 191–198.
- [43] A. Dukhin, S. Dukhin, P. Goetz, Electrokinetics at high ionic strength and hypothesis of the double layer with zero surface charge, *Langmuir: ACS J. Surf. Colloids*, 21 (2005) 9990–9997.
- [44] R. Zimmermann, U. Freudenberg, R. Schweiß, D. Kuttner, C. Werner, Hydroxide and hydronium ion adsorption — a survey, *Curr. Opin. Colloid Interface Sci.*, 15 (2010) 196–202.
- [45] B.D. Coday, D.M. Heil, P. Xu, T.Y. Cath, Effects of transmembrane hydraulic pressure on performance of forward osmosis membranes, *Environ. Sci. Technol.*, 47 (2013) 2386–2393.
- [46] M.S. Toran, A. D’Haese, I. Rodríguez-Roda, W. Gernjak, Fouling propensity of novel TFC membranes with different osmotic and hydraulic pressure driving forces, *Water Res.*, 175 (2020) 115657.
- [47] T.-T. Nguyen, R.S. Adha, R.W. Field, I.S. Kim, Extended performance study of forward osmosis during wastewater reclamation: quantification of fouling-based concentration polarization effects on the flux decline, *J. Membr. Sci.*, 618 (2021) 118755, doi: 10.1016/j.memsci.2020.118755.
- [48] J.C. Su, T.S. Chung, B.J. Helmer, J.S. de Wit, Understanding of low osmotic efficiency in forward osmosis: experiments and modeling, *Desalination*, 313 (2013) 156–165.
- [49] M. Xie, W.E. Price, L.D. Nghiem, M. Elimelech, Effects of feed and draw solution temperature and transmembrane temperature difference on the rejection of trace organic contaminants by forward osmosis, *J. Membr. Sci.*, 438 (2013) 57–64.
- [50] M.F.A. Goosen, S.S. Sablani, S.S. Al-Maskari, R.H. Al-Belushi, M. Wilf, Effect of feed temperature on permeate flux and mass transfer coefficient in spiral-wound reverse osmosis systems, *Desalination*, 144 (2002) 367–372.